MICROSTRUCTURAL INVESTIGATION OF PLASMA SPRAYED CERAMIC COATINGS USING PERIDYNAMICS

V. Guski[*1] **W. Verestek**[1] **E. Oterkus**[2] **S. Schmauder**[1]

1 Institute for Materials Testing, Materials Science and Strength of Materials
University of Stuttgart
Stuttgart, Germany

2 Department of Naval Architecture, Ocean and Marine Engineering
University of Strathclyde
Glasgow, United Kingdom

ABSTRACT

The present study deploys a continuum mechanics approach called peridynamics to investigate the damage behaviour of a 2D microstructure, which was taken from a plasma sprayed ceramic coating used in solid oxide fuel cell (SOFC) sealing systems. At the beginning, two benchmark cases, namely, plate with a hole as well as plate with a single edge notch, are considered. The results are compared to an analytical solution and a very good agreement is obtained. Based on these findings, a microstructural model from a plasma sprayed ceramic coating of SOFC sealing systems is investigated. These micromechanical simulations show that structural defects influence the crack initiation as well as the crack propagation during interconnecting the defects. Typical crack mechanisms, such as crack deflection, crack shielding or multiple cracking, are observed. Additionally, an anisotropy of the effective mechanical properties is observed in this heterogeneous material, which is well known for plasma sprayed materials.

Keywords: Bond-based peridynamics, plasma sprayed ceramic, damage modelling

1. INTRODUCTION

Numerical methods have increased their importance in materials science and mechanical engineering with increasing computational power during the last decades. Widely used numerical approaches are e.g. the finite element method (FEM) as a classical continuum mechanics approach or molecular dynamics (MD) in the nanometer range. FEM is a local, mesh-based method, which represents the treated component with a fixed mesh. It is usually chosen to simulate e.g. deformation of components or the mechanical behaviour of micro- or meso-structures. This approach has the advantage of highly accurate results of complex numerical problems with reasonable computational effort. However, due to these characteristics modelling of discontinuities e.g. crack initiation and crack growth increases the numerical effort. On the other hand, MD is a non-local simulation approach, which represents each atom or molecule by a discrete particle. The interaction between those particles is defined by a so-called potential function. The movement of each atom is based on Newton's equations of motion. The advantage of MD is the modelling of discontinuities in a natural way just by increasing the distance between two neighbouring atoms due to deformation. However, this high accuracy on the nano scale increases the computational effort dramatically.

The present study uses a rather new continuum mechanics approach called peridynamics (PD) that can be used with a mesh or a meshless approach [1]. PD is used to investigate the damage behaviour of a complex microstructure, which was taken from a plasma sprayed ceramic coating used in SOFC sealing systems. Plasma spraying is a typical industrial manufacturing procedure to produce ceramic coatings time and cost effective and is widely used for producing thermal barrier coatings on turbine blades for power generation or aircraft engines [2, 3].

Peridynamics combines the advantages of FEM and MD by representing components or microstructures, but with a non-local approach, that enables the modelling of discontinuities naturally. Especially on the microstructure scale several discontinuities exist, that can be represented by peridynamics. De Meo *et al*. (2016) and Wang *et al*. (2017) show the potential of this method by investigating the damage due to corrosion in polycrystalline materials and the thermomechanical behaviour of electrode material, which is typically deployed in solid oxide fuel cells, respectively [7, 8].

Due to the novelty of this approach, the study starts with

* Corresponding author (vinzenz.guski@imwf.uni-stuttgart.de)

DOI : 10.1017/jmech.2019.58

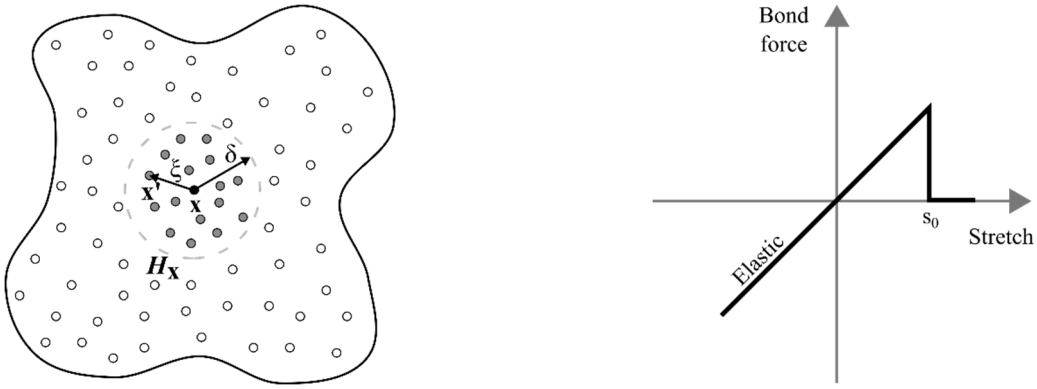

(a) (b)

Figure 1 Schematic representation of the function principle of peridynamics (a) and the linear elastic constitutive model with fracture at the critical stretch s_0 (b).

a benchmark procedure. Two different cases are selected to validate the resulting stress distribution on the one hand and to compare the damage behaviour on the other hand. Both benchmark problems possess analytical expressions with an exact solution for the assumed boundary conditions. After completing the benchmark procedure peridynamics is applied on a complex, plasma sprayed microstructure to investigate the damage behaviour.

2. METHODS OF SOLUTION

For the simulation, bond-based peridynamics (PD) is used [4], a non-local generalization of continuum mechanics, with a focus on discontinuous solutions as they arise in fracture mechanics. Within the context of continuum mechanics methods, peridynamics is basically a reformulation of the equation of motion in solid mechanics. In the bond-based PD theory the acceleration of each material point can be obtained by taking into account all the interactions associated with the material point **x**.

$$\rho(\mathbf{x})\ddot{\mathbf{u}}(\mathbf{x},t) = \int_{H_x} \mathbf{f}\left(\mathbf{u}(\mathbf{x}',t)-\mathbf{u}(\mathbf{x},t),\mathbf{x}'-\mathbf{x}\right)dV_{\mathbf{x}'} + \mathbf{b}(\mathbf{x},t) \tag{1}$$

where H_x represents the area or volume of the horizon and $\boldsymbol{b}$ refers to the body force density. The interactions are given by the pairwise force density **f** as spring forces between pairs of material points. These interactions only depend on the relative displacement (and potentially its history) of the interacting points and are thus independent of other points. Figure 1 (a) depicts the non-local representation in peridynamics. The interactions of the nodes are considered within a well defined region $\boldsymbol{H_x}$. This region is determined by the so called horizon δ, which is the radius of this region. The stretch of a bond can be calculated with the initial bond length ξ (= **x'** - **x**) and the relative displacement η (= $\boldsymbol{u}$(**x'**, *t*) - $\boldsymbol{u}$(**x**, *t*)) as

$$s = \frac{|\xi+\eta|-|\xi|}{|\xi|} \tag{2}$$

The parameter, which defines the spring forces is the so called bond constant *c*. A linear elastic isotropic material model is well defined for this bond-based approach due to the following expression of the pairwise force function

$$\mathbf{f} = \frac{\xi+\eta}{|\xi+\eta|} c\left(s-\alpha T_{avg}\right)\mu(t,\xi), \tag{3}$$

where α is the coefficient of thermal expansion, T_{avg} is the average temperature of the material points **x** and **x'** and μ is the failure parameter of the peridynamic bond, which is in the range between 0 and 1 and describes the state of the bond. The corresponding linear elastic material behaviour with brittle fracture is revealed in Figure 1 (b).

Generally, peridynamics is able to simulate 2D (2-dimensional) as well as 3D (3-dimensional) problems. Each dimensionality leads to a certain derivation of the final equations. In the framework of this study only 2D problems are considered. The corresponding bond constant *c* is linked to the Young's modulus E, the horizon δ and the model thickness t in the 2D case by the following expression [6].

$$c = \frac{9E}{\pi t \delta^3} \tag{4}$$

Due to the derivation of the bond constant *c* in equation (4) a fixed Poisson's ratio ν of 1/3 as well as the relations K = E/2(1-ν) and K = 2G are considered. The damage behaviour is triggered by a critical stretch s_0, which has to be reached to initiate damage. This damage parameter is directly linked to the strain energy release rate G_c and can be calculated with the horizon δ by the following equation [6].

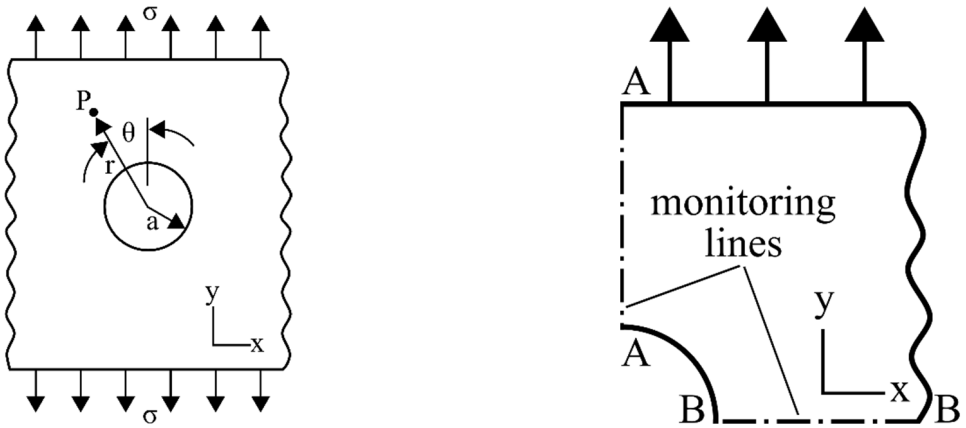

(a) (b)

Figure 2 Schematic representation of the first case: plate with a hole under uniaxial tension (a) and the region of interest to evaluate the results, including the positions of monitoring lines along the symmetry axes to generate displacement and stress profiles (b).

$$s_0 = \sqrt{\frac{4\pi G_c}{9E\delta}} \tag{5}$$

Here, the above mentioned constraints hold for the derivation of the critical stretch in Equation (5). Choosing an appropriate value for the parameter *horizon* is crucial to obtain reasonable simulation results with an acceptable computational effort. On the one hand, if the value is chosen too small, the accuracy of the solution can be low. On the other hand, a large value leads to high accuracy while the computational effort due to the large number of interactions is significantly large. It is obvious that the minimum value of the horizon size shall be the distance between the nearest particle neighbours. This distance is also known as discretization size. Previous studies from Silling and Askari (2005) have obtained the best results with a horizon / discretization size ratio of 3 [5]. This leads to a horizon, which includes all the particles within a distance of three nearest neighbour distances. For the simulations the peridynamics module in the open-source molecular dynamics program LAMMPS [9, 10] was deployed. Here, the bond-based PD approach with a linear elastic isotropic constitutive model is represented by the so called Prototype Microelastic Brittle (PMB) model. Similar to the theoretical derivations, as input parameter the bond constant c, the horizon δ and the critical stretch s_o are required to describe the linear elastic isotropic material behaviour. Basically, a completely independent behaviour of the critical stretch of a given bond is assumed, which is a simplification in the PD theory. Hence, to take into account the difference in the damage behaviour due to tensile and compressive loading, as observed in real brittle materials, an additional material parameter $\tilde{\alpha}$ is introduced.

$$s_0^{'} = s_0 - \tilde{\alpha} s_{min} \tag{6}$$

This parameter $\tilde{\alpha}$ is a constant, which triggers the enhancement of strength by compressive strain while the minimum stretch s_{min} is generally compressive. Based on the investigations in [4, 5] this material parameter is defined as 1/4.

Due to the circular horizon and the single cubic discretisation the volumes of the points near the horizon surface are truncated depending on the position with respect to the centre of the horizon. Thus, the corresponding volume of these surface points has to be assigned proportionally. Considering this fact in the calculation, a modification of the particle volume with a linear unitless nodal volume scaling function is implemented to overcome this discrepancy of the circular horizon and the single cubic discretisation.

3. RESULTS AND DISCUSSION

In order to validate the PD theory implemented in LAMMPS software two benchmark cases are calculated and compared with FEM results and results from analytical solutions. These benchmark cases enable the validation of the deformation or stress distribution and the damage behaviour, respectively.

3.1 Case 1: Plate with a hole under uniaxial loading

The first case is used to validate the overall deformation behaviour with corresponding stresses. For this purpose, the simple case "plate with a hole under uniaxial tension" is selected. Figure 2 (a) shows the schematic representation of this case. The stress distribution as well as the displacement field can be expressed by an analytical solution, which was postulated by Kirsch in 1889 [11]. Due to the symmetries an evaluation of a quarter of the plate is sufficient. Thus, the considered part of the model to evaluate the results is shown Figure 2 (b). Besides, to be able to compare the analytical and the numerical results in detail, two monitoring lines are introduced to generate profiles of the

Table 1 Material properties and structural parameters for the simulation.

Young's Modulus E (GPa)	100
Poisson's ratio (-)	0.33
Density (kg/m³)	2200
Tension (MPa)	95
Strain energy release rate GIc (J/m²)	2
Discretization size x (m)	0.00075
Horizon (m)	0.00225
Thickness t (m)	0.00075
Particle volume V (m³)	0.422 x 10^{-9}

displacements and stresses along the symmetry axes.

In cylindrical coordinates the stress can be calculated in terms of loading and the radius a of the hole at the centre. The actual position at a certain point P on the plate is defined by the distance r from the centre of the hole and the angle between the symmetry axis in loading direction and the vector from the centre to the point P. In radial direction the stress is defined by the following equation.

$$\sigma_{rr} = \frac{\sigma}{2}\left(1-\frac{a^2}{r^2}\right)+\frac{\sigma}{2}\left(1-\frac{a^2}{r^2}\right)\left(1-\frac{3a^2}{r^2}\right)cos2\theta \qquad (7)$$

A similar expression for the stress in tangential direction can be written as

$$\sigma_{\theta\theta} = \frac{\sigma}{2}\left(1+\frac{a^2}{r^2}\right)-\frac{\sigma}{2}\left(1-\frac{3a^4}{r^4}\right)cos2\theta \qquad (8)$$

Finally, the stress in shear direction can be written as

$$\sigma_{r\theta} = -\frac{\sigma}{2}\left(1-\frac{a^2}{r^2}\right)\left(1+\frac{3a^2}{r^2}\right)sin2\theta \qquad (9)$$

In order to compare the calculated stress with the numerical results the coordinate system was transformed from cylindrical coordinates to Cartesian coordinates. Due to this transformation the normal stress components in x and y directions and shear stress were calculated with the following equations.

$$\sigma_x = \sigma_r sin^2\theta + \sigma_\theta cos^2\theta + \sigma_{r\theta} sin2\theta \qquad (10)$$

$$\sigma_y = \sigma_r cos^2\theta + \sigma_\theta sin^2\theta - \sigma_{r\theta} sin2\theta \qquad (11)$$

$$\sigma_{xy} = (\sigma_r - \sigma_\theta) sin\theta cos\theta + \sigma_{r\theta} cos2\theta \qquad (12)$$

Finally, a reformulation of the previous equations was used to calculate the displacements in x and y direction.

$$u_x(r,\theta) = \frac{\sigma a}{8G}\left(\begin{array}{l}\frac{r}{a}(\kappa-3)sin\theta + \\ \frac{2a}{r}\left((1-\kappa)sin\theta + sin3\theta\right) - \frac{2a^3}{r^3}sin3\theta\end{array}\right) \qquad (13)$$

$$u_y(r,\theta) = \frac{\sigma a}{8G}\left(\begin{array}{l}\frac{r}{a}(\kappa+3)cos\theta + \\ \frac{2a}{r}\left((1+\kappa)cos\theta + cos3\theta\right) - \frac{2a^3}{r^3}cos3\theta\end{array}\right) \qquad (14)$$

where $G = E/2(1+\nu)$ is the shear modulus and $\kappa = (3-\nu)/(1+\nu)$ is a constant. With these expressions the analytical solutions are obtained to compare with the numerical results using PD.

A full simulation model of the whole plate was set up. A radius a of 10 mm and a plate edge length of 200 mm was defined. Table 1 summarizes the material properties used as input parameters. Applying these data in equation (4) the bond constant c is calculated as 1.91 x 10^{23} Pa/m^4. The loading is displacement-controlled with a strain rate of 0.1 1/s. The whole model is surrounded by an additional boundary layer because surface correction is not available in LAMMPS. Furthermore homogenous displacement is only possible in periodic directions, therefore periodic boundaries are used in loading direction. The result is not influenced by this. In the second direction, perpendicular to the loading direction, free surfaces are used. An explicit simulation scheme was deployed with an increment of 1.0 x 10^{-7} s. Preliminary studies have delivered the simulation parameter to ensure quasi static conditions.

The FE model represents the quarter of the whole set up due to the symmetry according to the analytical model. A plane stress element type is selected for the FE mesh with an average element size of 0.2 mm. Along the symmetry axes only the degree of freedom perpendicular to the regarded axis is constrained as well as the rotational degrees of freedom. On the upper edge of the plate the displacement-controlled loading in Y direction was applied. The outer edge perpendicular to the loading direction and apart from the symmetry axis is considered as a free surface.

Calculating the analytical solution with the input parameters above leads to the displacement field depicted

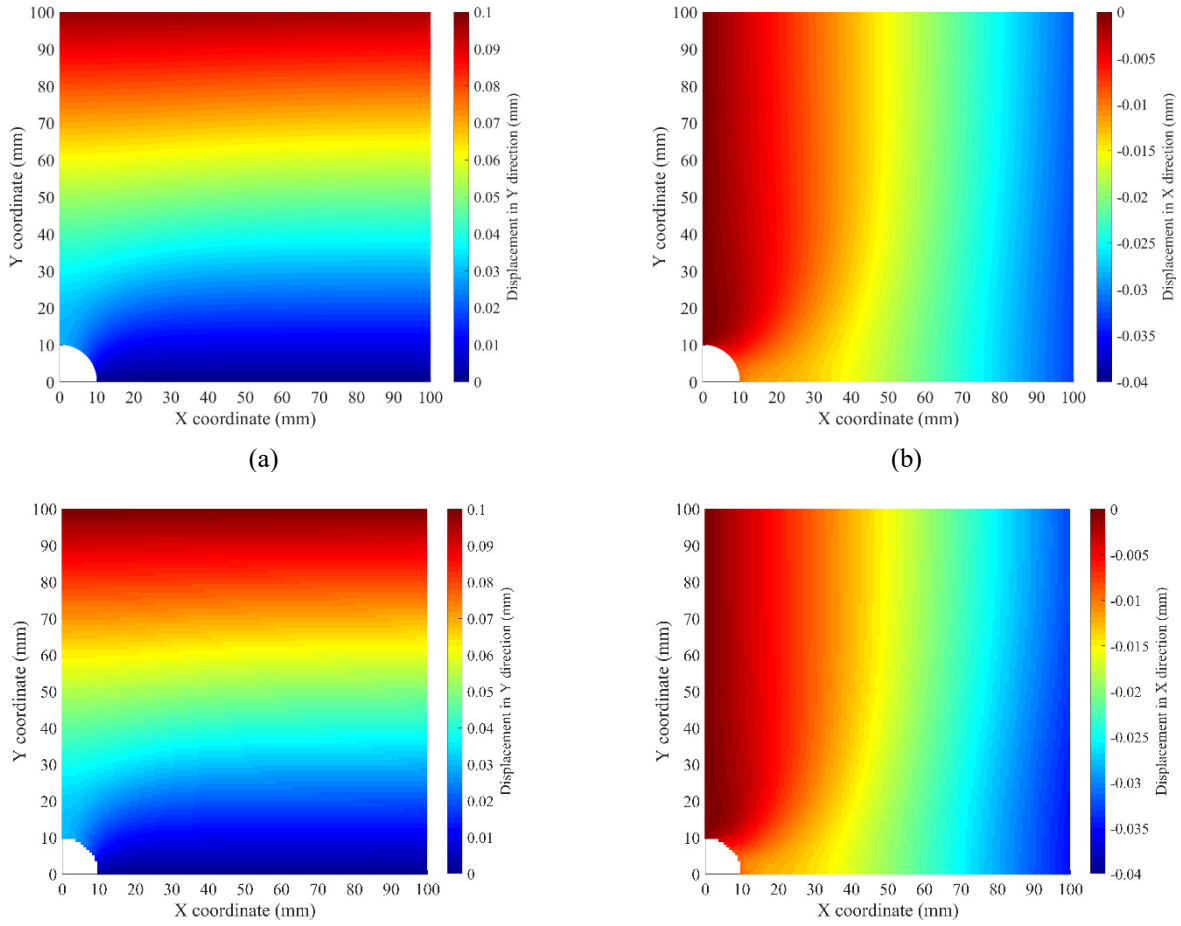

Figure 3 Displacement field in loading direction (a) and perpendicular to the loading direction (b) calculated by the Kirsch equation and the corresponding PD results in loading direction (c) and perpendicular to the loading direction (d).

in Figs. 3 (a) and (b). Due to the symmetry of the sample only a quarter of the plate is shown. Lower stiffness due to the hole at the centre of the sample increases the displacement in loading direction Y in front of the hole (Fig. 3 (a)). The free surface on the sample edge perpendicular to the loading direction apart from the symmetry axis leads to contraction of the sample in X direction (Fig. 3 (b)). The corresponding PD results are shown in Figures 3 (c) and (d). The displacement fields match quite well with the analytical results.

Knowing the displacement field and the Young's modulus for a linear elastic material one can calculate the stress distribution. Figure 4 shows the resulting stress field of the analytical solution as well as the PD results. For PD the stress at each material point is obtained by utilizing the compute pressure function without the kinetic energy part, which is provided by LAMMPS [9]. A maximum stress of 285 MPa is obtained in loading direction adjacent to the hole at the symmetry axis (Fig. 4 (a)). In front of the hole a stress free region occurs. Perpendicular to the loading direction the obtained stress level is lower. The maximum stress in X direction is localized at an angle of 45 ° on the edge of the hole. The previous observations in the displacement fields coincide with the comparison of the stress field. The overall stress field is very comparable to each other.

In order to validate the numerical results more in detail, the displacements as well as the stresses parallel and perpendicular to the loading direction are compared along the symmetry axis. The locations of the monitoring lines correspond to the sketch in Figure 2 (b). Figure 5 depicts the displacement profiles in both directions of the FE as well as the PD results and the results from the analytical solution. With the applied boundary conditions, for the displacements in loading direction (Fig. 5 (a)) a good match of all results is observed. Only a slight deviation between the results of the analytical solution and the numerical results is noticed. The deviation can be attributed to the assumptions in the analytical solution, which consider an infinite extent perpendicular to the loading direction. Due to the numerical effort, a cut off length was determined in preliminary studies, which ensures a sufficient accuracy with feasible calculation time. However, in the vicinity of the hole the difference in the displacements are negligible.

Due to the peridynamics algorithm, a proper particle volume is needed to calculate the stress distribution.

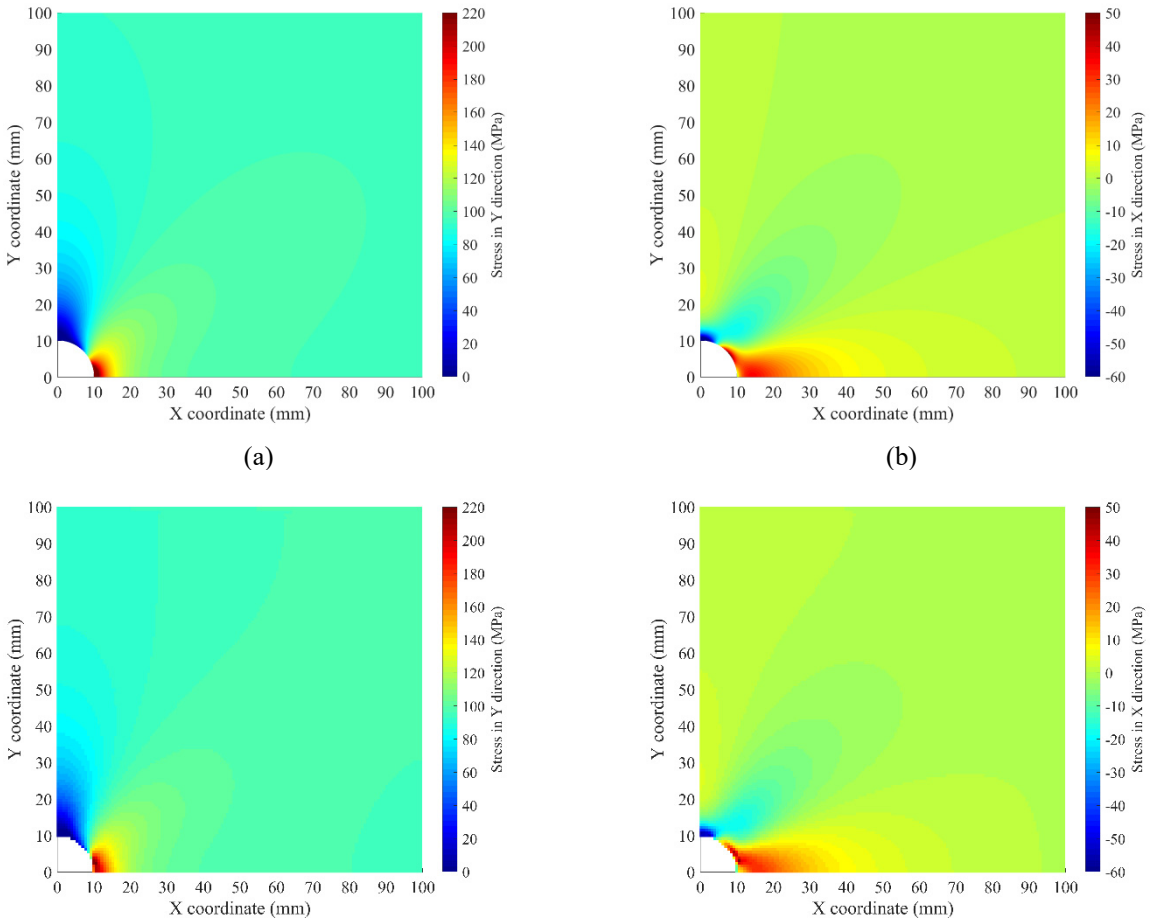

Figure 4 Stress field in loading direction (a) and perpendicular to loading direction (b) calculated by the Kirsch equation and the corresponding PD results in loading direction (c) and perpendicular to the loading direction (d).

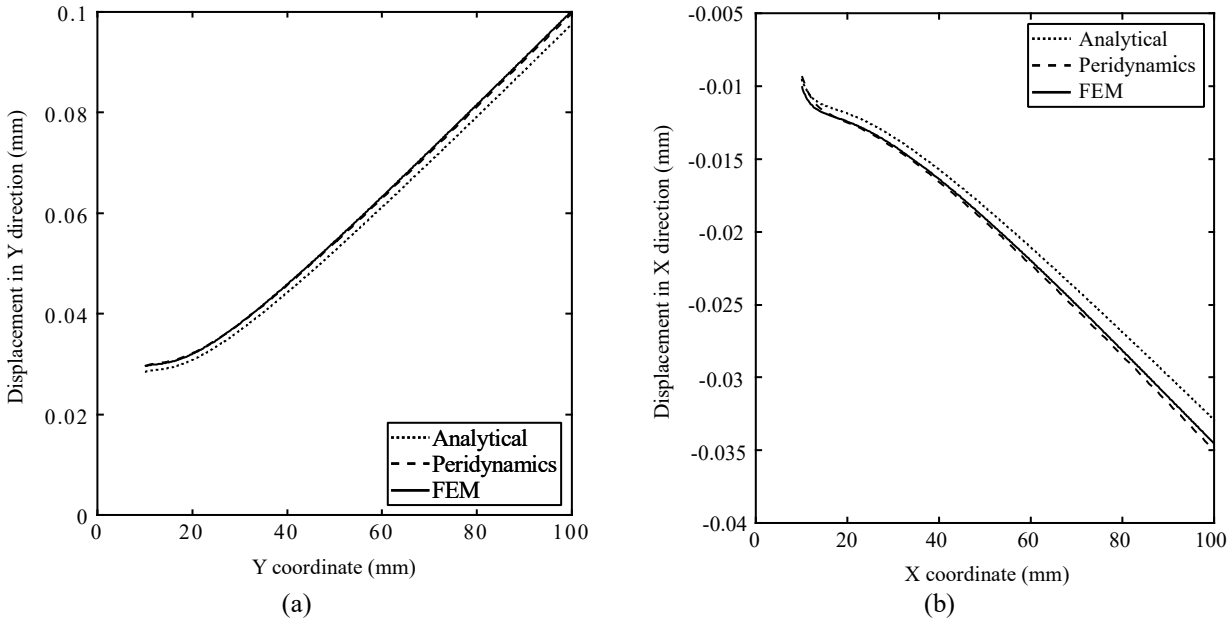

Figure 5 Comparison of the displacement profile in loading direction (A-A) along the monitoring line A-A (a) and perpendicular to the loading direction (B-B) along the monitoring line B-B calculated with analytical model, FEM and peridynamics (see monitoring lines A-A and B-B in Fig 2 (b)).

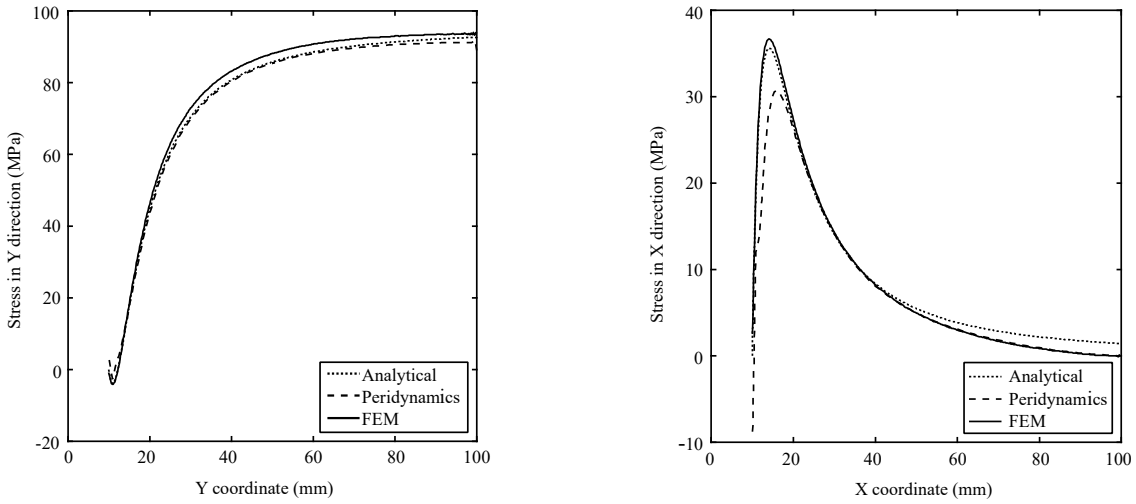

Figure 6 Comparison of the stress profile in loading direction (A-A) along monitoring line A-A (a) and perpendicular to the loading direction (B-B) along monitoring line B-B calculated with analytical model, FEM and peridynamics (see monitoring lines A-A and B-B in Fig 2 (b)).

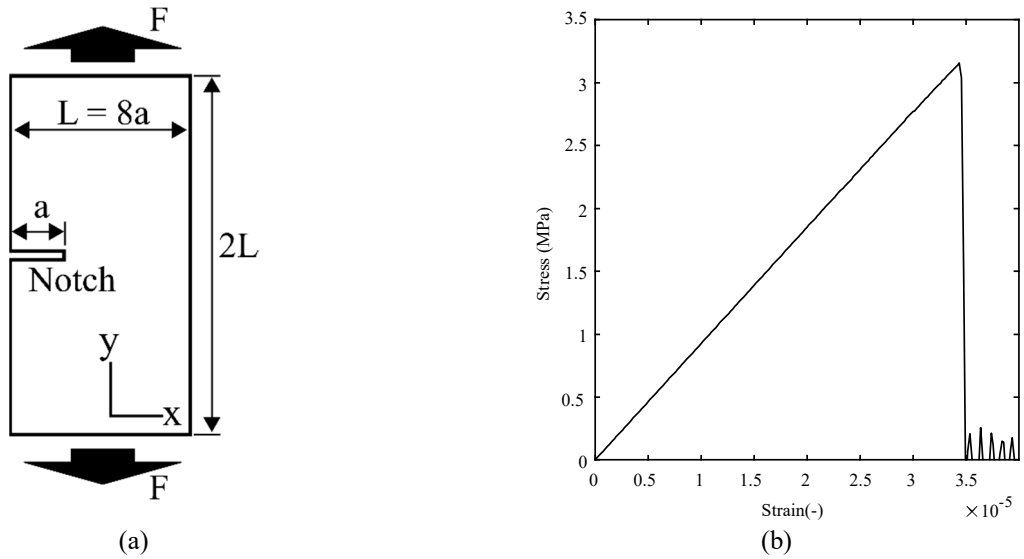

Figure 7 Schematic representation of the second benchmark case: plate with a single-edge notch under uniaxial tension (a) and the resulting stress-strain curve of the PD simulation (b).

Typically, a particle volume, which is the cubic of the lattice constant, is deployed (see Table 1). Figure 6 shows the stress profiles along the symmetry axes parallel (a) and perpendicular to the loading direction (b). The shapes of the profiles coincide well. In figure 6 (a) a good match of the peridynamics results with the analytical results is observed. However, in the stress profile of the stress in X direction in Figure 6 (b) an underestimation near the hole is obtained. The deviation of the maximum shear stress is caused by the assumptions of the relation between bulk modulus and shear modulus in the derivation of the PMB constitutive model. This shear behaviour is not straightforward to be reproducible by the constitutive models of the analytical solution as well as the FE model, which is based on the classical derivation of linear elastic isotropic material behaviour. The slight underestimation of the stress apart from the hole is caused by the finite size of the numerical models in contrast to the assumption of an infinite extent of the analytical model, which already indicates the displacement profile in figure 5 (b).

Considering the aforementioned particle volume over the whole sample the results match quite well. Attention should be paid on the shear behaviour of the utilized PMB constitutive model, which delivers slightly different stresses perpendicular to the loading direction due to the fixed Poisson ration in the derivation of the PMB constitutive model. With these insights the validation of the peridynamics approach was successful with respect to the calculated stress distribution. The following second benchmark case focuses on modelling macroscopic damage behaviour.

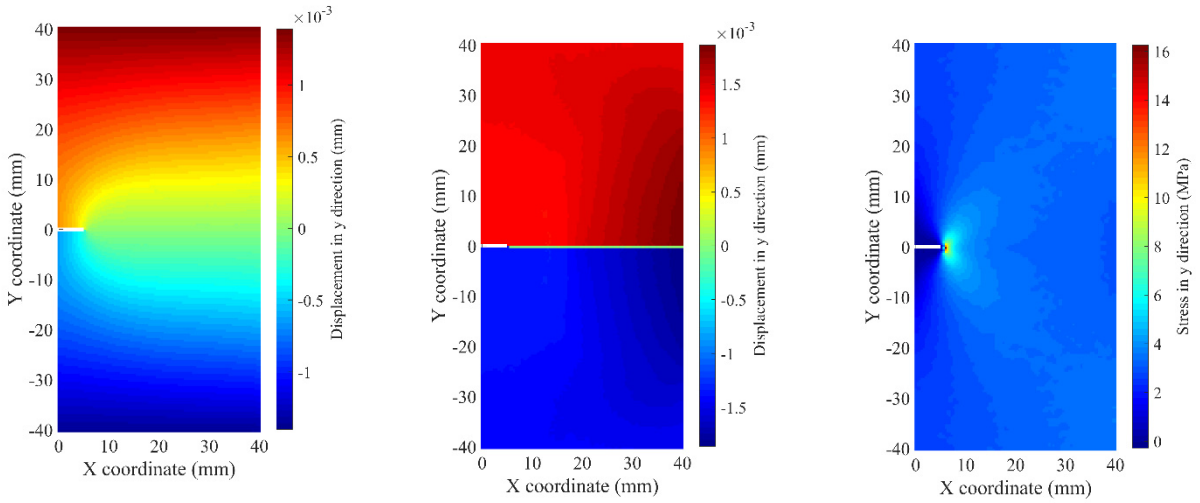

Figure 8 Resulting contour plot of displacement in loading direction at crack initiation (a) and after cracking (b) and the contour plot of stresses in loading direction at crack initiation (c).

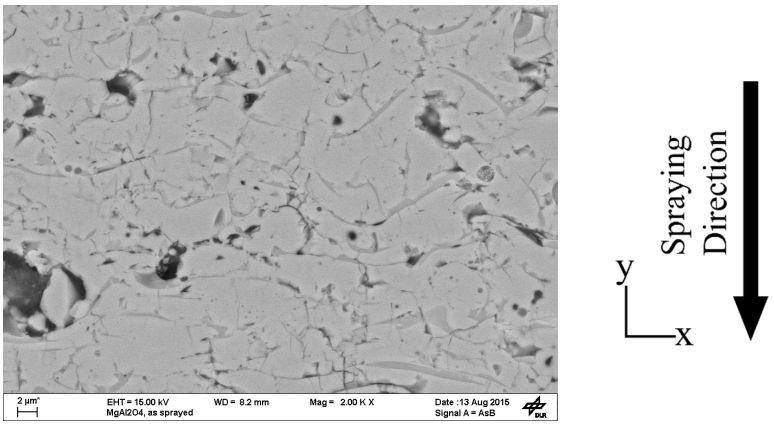

Figure 9 Cross-section of a plasma sprayed Mg spinel coating (source: DLR, Stuttgart).

3.2 Case 2: Plate with a single-edge notch

A schematic representation of the plate with a single edge notch is shown in Figure 7 (a). According to [12] an analytical expression exists, which allows the calculation of the fracture stress under a certain ratio of notch length a and plate width L. The comparison of the fracture stress by keeping the previous boundary conditions of the PD simulation fixed allows an adjustment of the critical stretch s_0 in the peridynamics model. Again, an explicit simulation scheme was deployed with a time increment size of 1.0×10^{-7} s. The discretization size was set to 0.0004 m. Figure 7 (b) depicts the resulting stress-strain curve of the PD simulation. A maximum stress, which is the fracture stress, of 3.16 MPa was observed.

In order to evaluate the simulation results, the moment of crack initiation was determined. Then, the results at that time are compared with the analytical solution. Figure 8 shows contour plots of the displacements and stresses in loading direction at crack initiation and after cracking. The contour plot of the displacements in figure 8 (a) shows the deformation of the plate in positive and negative Y direction, respectively. Figure 8 (b) shows the final configuration of the cracked sample. The plate is separated into two parts due to the crack, which is indicated by the uniform red and blue colour of the upper and lower parts, respectively. The maximum stress at the crack tip is determined with 16.25 MPa, which depicts Figure 8 (c). Finally, the fracture stress is validated by comparison with the analytical solution.

The fracture stress can be calculated according to [12] based on linear elastic fracture mechanics (LEFM):

$$\sigma_F = K_{Ic} \frac{1}{\sqrt{\pi a}} \left(\begin{matrix} 1.12 - 0.23\frac{a}{L} + 10.6\frac{a^2}{L^2} \\ -21.7\frac{a^3}{L^3} + 30.4\frac{a^4}{L^4} \end{matrix} \right)^{-1} \tag{15}$$

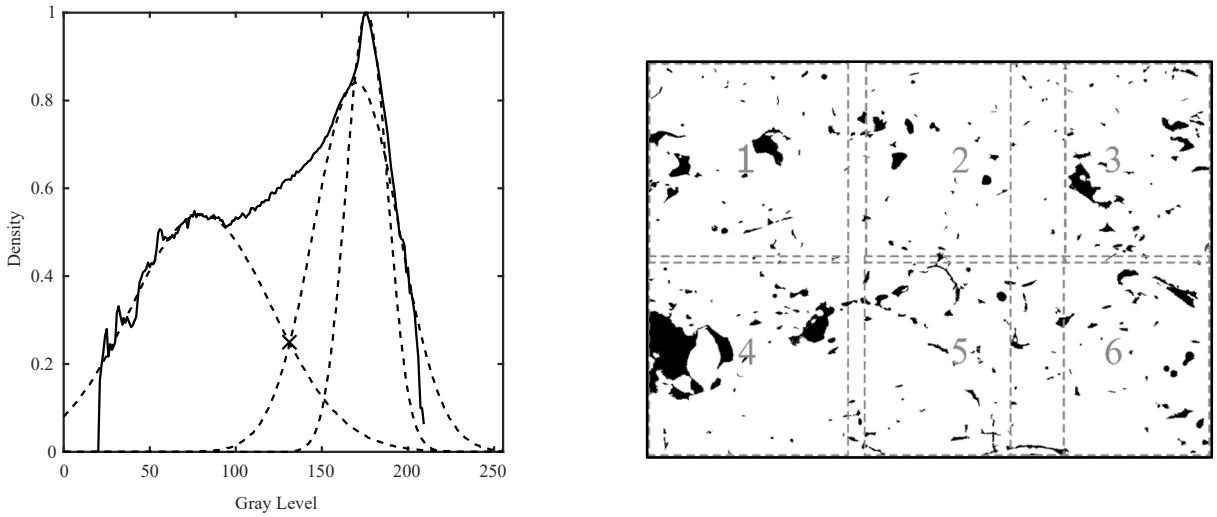

(a) (b)

Figure 10 Histogram with applied minimum value method with an identified grey scale threshold value of 131 (a) and the corresponding binarized image with the different cutout positions.

where K_{Ic} is the fracture toughness, which can be calculated from the strain energy release rate. Assuming an initial notch length a = 4 mm, a fracture stress of 3.1 MPa is thus obtained. From the peridynamics simulation, a fracture stress of 3.16 MPa is obtained by applying a critical stretch s_0 of 0.13 x 10^{-3}, which is derived using equation (5).

Concluding both benchmark simulations, a good reproducibility of the stress distribution as well as the damage behaviour with peridynamics is observed. However, attention has to be paid on the shear behaviour of the PMB material model, which leads to a slight underestimation of the calculated stresses. With these results, the numerical method is proved on the continuum level and the following microstructure-based investigations are conducted.

3.3 Microstructure-based Simulation

The microstructural approach reveals relevant mechanical properties of the plasma-sprayed coating by taking into account the characteristic microstructural features such as pores or microcracks and their orientation. Figure 9 shows a SEM image used to investigate fine cracks and pores in the microstructural simulation. The SEM image magnification is 2000 x and the micrograph size is 1024 x 768 pixels in the treated image corresponding to a pixel edge length resolution of 0.11 µm/px. By visual inspection, three main phases can be distinguished. The largest area is filled with a light grey color and represents the bulk material. The black area indicates the pores and cracks in the microstructure. Besides, a third phase characterized with dark grey pixel is detected. This secondary phase is distributed over the whole microstructure in a wavy manner. It seems that this, so called contact zone, covers each splat layer. Therefore, it is assumed that this phase with a different concentration or density arises due to solidification and remelting during the spraying process. In this image the spraying direction is in y direction. From literature, it is well known that the spraying direction influences the effective material properties significantly [15, 16].

A fundamental step in this microstructural approach is the conversion of the greyscale $MgAl_2O_4$ SEM images into binary images by applying a subsequent brightness threshold technique. The threshold value controls the grey values and therefore describes the amount of pores in the numerical model. Several techniques to determine an adequate grey scale value threshold are reported in literature [13]. The most straightforward method is the visual comparison of the binary image with the original image. The threshold is adjusted until the best match of both images is reached. Another method uses the measured porosity as a parameter to fit the threshold until the same porosity can be calculated for the binary image. Further, more advanced, methods analyse the grey scale value distribution of the original image in more depth. Such types of procedures are e.g. the tangent method and the minimum value method. In the framework of this study the minimum value method, which was postulated by Tsai, is selected [14]. As a result of this procedure, the treated images consist of black and white pixels corresponding to the pores and cracks and the matrix phase, respectively. This so called segmentation procedure delivers the geometry for the simulation model. The grey scale value ranges from 0 to 255 representing the colour black at the grey scale value 0 and white at 255. The shape of the grey scale value distribution is similar to a normal curve with a maximum in the range of the grey scale values between 150 and 200 (Figure 10 (a)). A closer look on the shape of the distribution curve reveals that it can be approximated by three Gaussian curves (dashed lines), where each curve corresponds to one phase in the image. The first Gaussian with a maximum around grey scale value 75 corresponds to cracks and pores. The second curve with its maximum around 160 belongs to the splat interphases and the third Gaussian curve with a maximum around 175 belongs to the ceramic

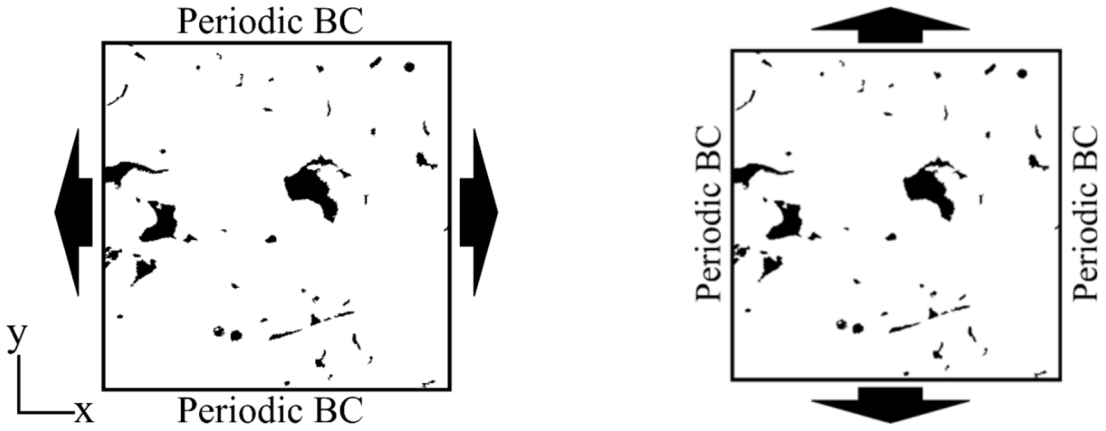

Figure 11 Schematic representation of the constraints and boundary conditions of the PD simulation models with loading in x direction (a) and loading in y direction (b).

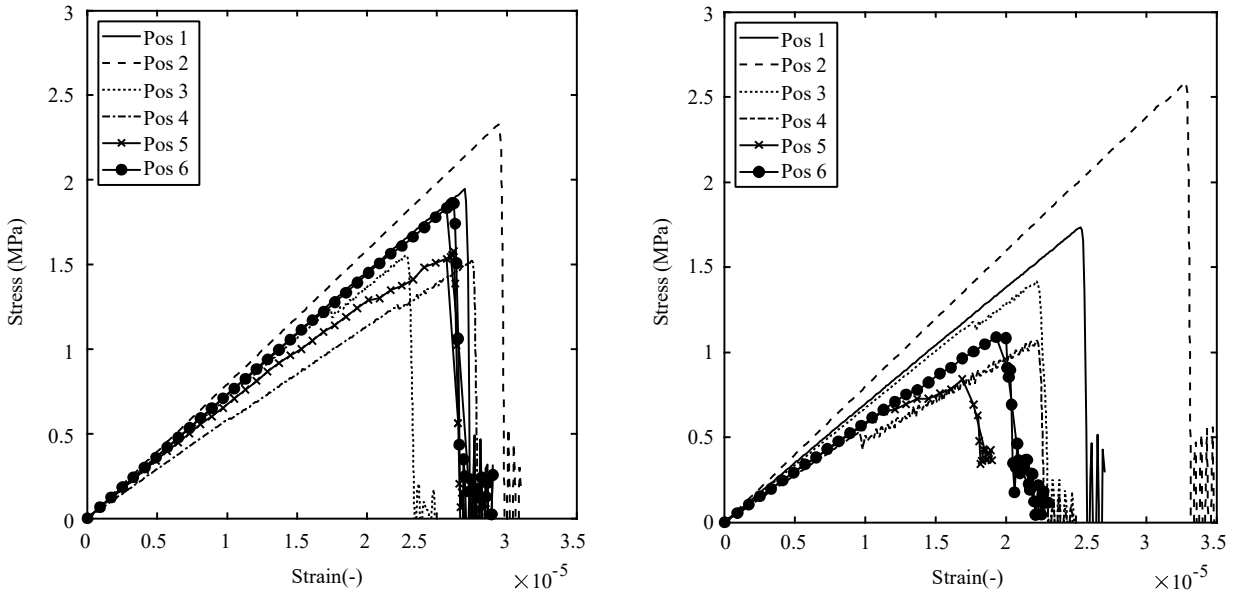

Figure 12 Resulting stress-strain curves of the frames loaded in X direction (a) and loaded in Y direction (b) according to the boundary conditions in Fig. 11

phase itself. Figure 10 (a) shows the application of the so called minimum value procedure [14]. The intersection of the first and the second fitted curve was identified and the corresponding grey scale value was determined with a grey scale threshold value of 131 and applied in the segmentation procedure. The resulting binarized image with the threshold 131 is presented in figure 10 (b). Applying the threshold in the segmentation procedure on the SEM image a binarized image with a porosity of 5.4 % is obtained, which matches the measured porosity of 4 % to 6 %. The visual inspection leads to a good agreement with the original SEM image in figure 9.

In order to establish the simulation model, the prepared binary image is divided into quadratic frames. Each frame is deployed as one simulation model with an edge length of 20 µm. A frame at position 1 is shown in Figure 11 (a) as an example. In total, six frames are extracted from the binarized image and are deployed for further investigations. The discretization size of the simulation models was set to 0.0005 m. Periodic boundary conditions and uniaxial tensile loading in x- and y-directions are applied to the simulation models as shown in Figure 11. An explicit simulation scheme was deployed with an increment size of 1.0×10^{-7} s similar to the benchmark simulations. The material parameters such as the bond constant $c = 1.91 \times 10^{23}$ Pa/m^4 and the critical stretch $s_0 = 0.13 \times 10^{-3}$ are taken from the benchmark simulations, too. In order to analyse the anisotropic behaviour of the plasma-sprayed coating the simulations with different loading directions are compared. Considering the findings of the benchmark simulations only the stresses in loading direction are evaluated.

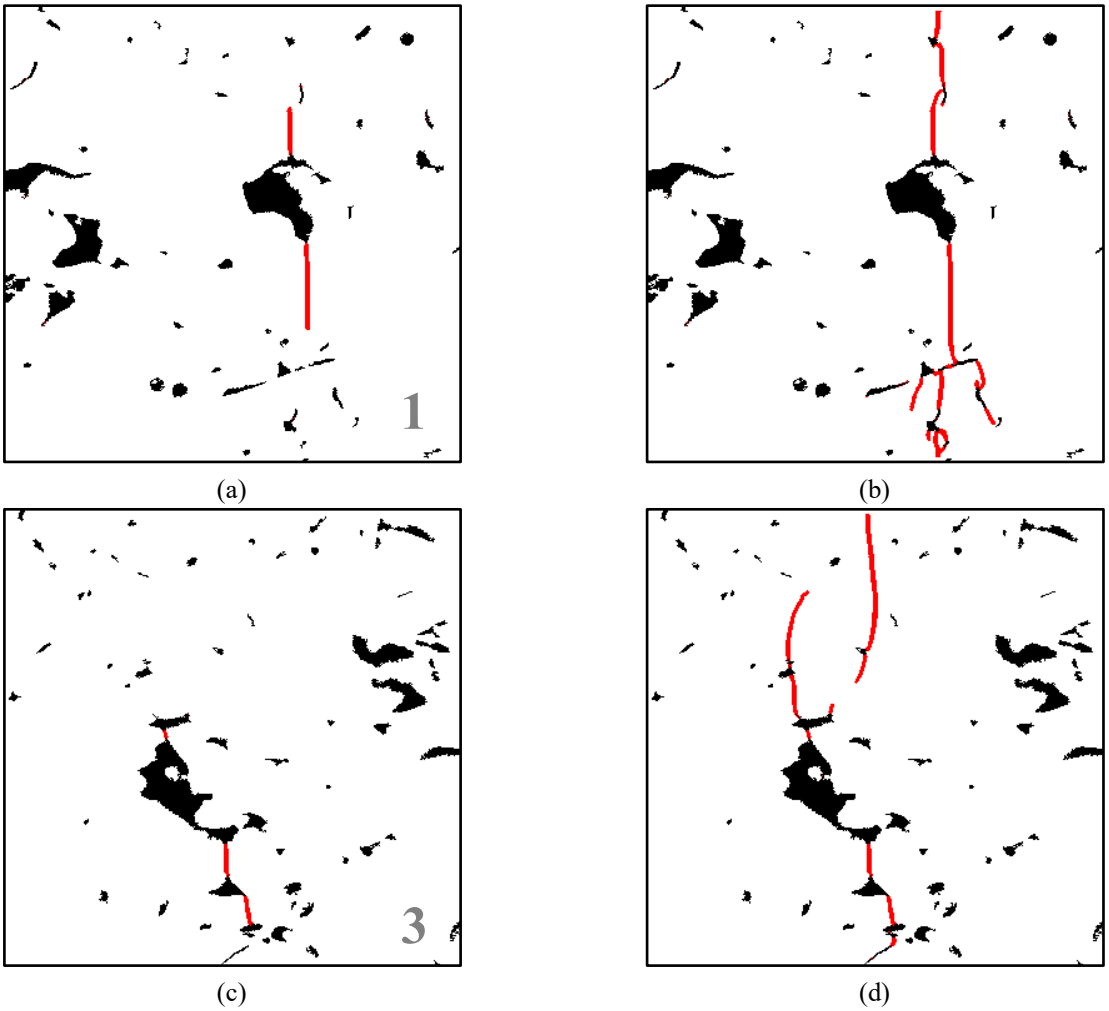

(a) (b) (c) (d)

Figure 13 Resulting crack pattern of the microstructures of position 1 (a, b) and 3 (c, d) under uniaxial loading perpendicular to the spraying direction (in x direction) at different snapshots from the PD simulations.

Evaluating the microstructure models the resulting stress strain curves are compared with each other and the crack paths are analysed. The resulting stress-strain curves of all simulation models in x and y directions are shown in Figure 12. The stress-strain behaviour is in accordance to the material model (see Fig. 1 (b)) with a linear elastic slope until cracking occurs. After cracking a sudden dropdown to a stress free state and stress oscillations are observed (Fig. 12). An anisotropic behaviour is observed, as indicated by the lower maximum stress of the results with applied loading in y direction (Fig. 12 (b)).

In summary, the crack paths for each simulation model and loading direction at every snapshot are analysed. As expected, the structural defects promote the crack initiation in several locations. With further loading, exposed lying cracks start to grow. Finally, these cracks interconnect the structural defects perpendicular to the loading direction until the crack divides the whole structure into two parts, mostly. In each microstructure, the applied tensile loading results in the shortest crack path through the simulation model by interconnecting the initial crack like pores. However, not only one straight crack appears but also crack branching is observed adjacent to clustered initial crack like pores. Besides, multiple crack initiation and side crack activities occur in the microstructure. These observations are typical for plasma sprayed ceramics and are proved by the investigations of Malzbender *et al.* [17] on the fracture behaviour of plasma sprayed thermal barrier coatings.

In order to analyse the damage behaviour of the plasma-sprayed material the crack pattern at different snapshots are evaluated in detail. Exemplarily, the frames of position 1 and position 3 with both loading conditions are selected for further evaluation. The crack pattern of the microstructures loaded in x direction are depicted in Figure 13. Figure 13 (a) and (c) show snapshots immediately after crack initiation. In both cases the initiation occurs at the largest void in the centre of the frame on the upper and lower edge. The cracks grow straight in both directions perpendicular to the loading direction until adjacent voids in the crack path are reached. Then, the cracks move through these voids and proceed growing at the opposite edges. Due to periodic boundary conditions and different starting points of the crack initiation, the cracks move through the boundary

Table 2 Simulation results with porosity and effective Young's modulus.

Frame	Porosity (%)	$E_{\perp}$ (GPa)	$E_{\parallel}$ (GPa)	$E_{\perp} / E_{\parallel}$
Position 1	4.2	67.1	64.2	1.05
Position 2	2.3	75.1	73.9	1.02
Position 3	4.5	62.2	56.8	1.10
Position 4	11.5	52.6	42.8	1.23
Position 5	4.0	58.4	44.3	1.32
Position 6	4.2	64.2	48.5	1.32

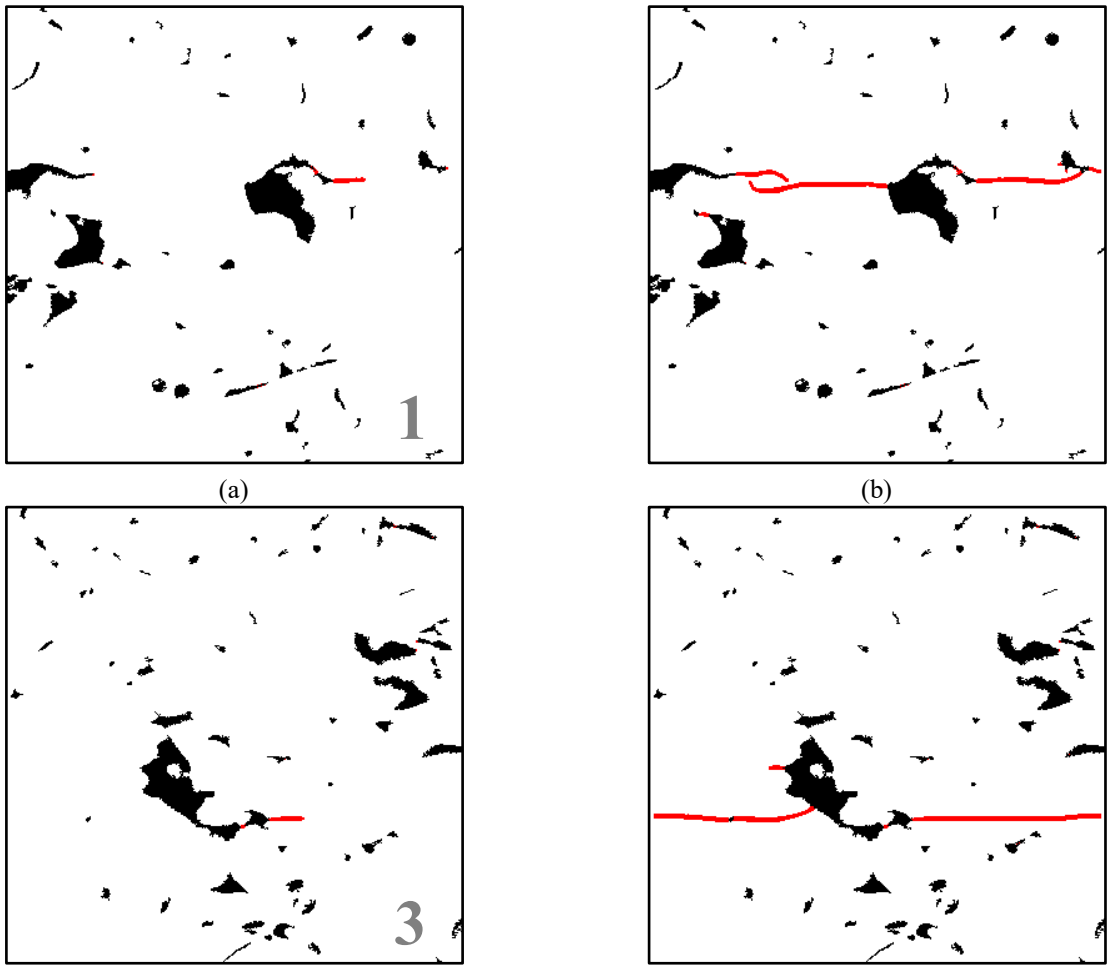

(a) (b) (c) (d)

Figure 14 Resulting crack pattern of the microstructures of position 1 (a, b) and 3 (c, d) under uniaxial loading parallel to the spraying direction (in y direction) at different snapshots from the PD simulations.

and appear on the opposing side. This effect leads to a straight crack through the whole microstructure (Fig. 13 (b)) or to a crack path with an offset (Fig. 13 (c)). Latter observation leads to crack shielding, which lock the crack due to energy dissipation. Besides, typical mechanisms as multiple cracking and void deflection are observed in Figure 13 (b).

Figure 14 shows the crack pattern of the same microstructures but loaded in y direction at different snapshots. The evaluation of the crack pattern immediately after crack initiation in (a) and (c) delivers that crack initiation occurs at the same large void in the centre of the frame. In contrast to the microstructures, which are loaded in x direction, the initiation sites appear only on the right edge of the voids. In both microstructures, the cracks grow through the boundary and appear on the opposing edge. Again, crack shielding is observed (Fig. 14 (b)).

The stiffness of each model corresponds to its porosity. With increasing porosity, a decrease of the effective Young's modulus and maximum stress is observed. Besides, a scatter of the maximum stress is observed, which is typical for brittle materials. Table 2

summarizes the porosities of the frames and the resulting effective Young's moduli. The analysis of the porosity delivers an intermediate porosity of position 1, position 3, position 5 and position 6, a low porosity of position 2 and a high porosity of position 4. Besides, a measure for the anisotropy, the ratio of Young's moduli perpendicular and parallel, is calculated and shown in this table. A mean value of 1.17 slightly underestimates the investigations of Wang *et al*. [15, 16] on the anisotropic material behaviour of plasma sprayed ceramic coatings. However, from literature it is known that a so called contact zone between the single splats exists in plasma sprayed materials [18]. This contact zone possesses a weaker material behaviour compared to the bulk material. Due to the different distribution parallel and perpendicular to the spraying direction along the splats an enhanced anisotropic behaviour is expected [19]. Further studies will take into account such a secondary phase.

4. CONCLUSIONS

In this study, microstructural investigations were performed using bond-based peridynamics. The complete workflow beginning at the SEM image, the image analyses for binarization and the final simulation model with the numerical results were presented. In order to validate the simulation method, two benchmark cases, which possess analytical expressions, were chosen and compared with other numerical and analytical results successfully. These benchmark cases cover the stress distribution (plate with a hole under uniaxial loading) as well as the damage behaviour with the fracture stress (plate with a single edge notch). The microstructural investigations on six different frames deliver a well known anisotropic behaviour of the plasma-sprayed ceramic coating, although the typical contact zone in between the single splats, which is assumed to have a weakening effect on the plasma-sprayed coating, was not yet taken into account in the simulation. This leads to the conclusion that the consideration of such a secondary phase can enhance the anisotropic behaviour further. In this study, the observed anisotropic behaviour is caused by the characteristic nonuniform shape of the larger voids in the coating, which appear due to shrinkage of the splats during the production process. The resulting crack path in each frame was analysed in both loading directions. As expected, these results show that the structural defects influence the crack path significantly as well as the crack propagation by interconnecting the defects. Further studies will focus on the effect of such a contact zone in the plasma-sprayed coatings on the anisotropic behaviour.

ACKNOWLEDGEMENTS

This work was conducted with financial support of German Ministry of Education and Research (BMBF) for project "SHEACOAT" under grant no. WING-13X4012B and of the German Research Foundation (Deutsche Forschungs Gemeinschaft, DFG) under grant no. Schm 746/166-1. Contributions of Dr. Sata providing the SEM image as well as scientific support from Dr. Ansar are acknowledged. The authors acknowledge support by the state of Baden-Württemberg through bwHPC.

NOMENCLATURE

E	Young's modulus, N/m^2;
K	bulk modulus, N/m^2;
G	shear modulus, N/m^2;
σ_F	fracture stress, N/m^2;
G_{Ic}	strain energy release rate, J/m^2;
K_{Ic}	fracture toughness, $MPam^{-1/2}$;
ν	Poisson's ratio;
δ	horizon, m;
t	thickness, m;
x	discretization size, m;
c	bond constant, N/m^6;
V	particle volume, m^3;
s_0	critical stretch, m/m;
T_{avg}	average temperature, K;
α	thermal expansion coefficient, 1/K;
ρ	density, kg/m^3;
μ	failure parameter;
$\tilde{\alpha}$	material parameter;

REFERENCES

1. Chen, X. and Gunzburger, M., "Continuous and Discontinuous Finite Element Methods for a Peridynamics Model of Mechanics," *Computer Methods in Applied Mechanics and Engineering*, 200(9-12), pp.1237-1250 (2011).
2. Padture, N. P., Gell, M. and Jordan, E. H., "Thermal Barrier Coatings for Gas-Turbine Engine Applications," *Science*, 296(5566), pp.280-284 (2002).
3. Xu, H., Guo, H. (Eds.), "*Thermal Barrier Coatings*," Woodhead Pub Limited (2011).
4. Silling, S. A., "Reformulation of Elasticity Theory for Discontinuities and Long-Range Forces," *Journal of the Mechanics and Physics of Solids*, 48(1), pp.175-209 (2000).
5 Silling, S. A. and Askari, E., "A Meshfree Method Based on the Peridynamic Model of Solid Mechanics," *Computers and Structures*, 83(17-18), pp.1526-1535 (2005).
6. Madenci, E. and Oterkus, E., "*Peridynamic Theory and its Applications"* (Vol. 17), New York: Springer (2014).
7. De Meo, D., Diyaroglu, C., Zhu, N., Oterkus, E. and Siddiq, M. A., "Modelling of Stress-Corrosion Cracking by using Peridynamics," *International Journal of Hydrogen Energy*, 41(15), pp.6593-6609

(2016).

8. Wang, H., Oterkus, E., Celik, S. and Toros, S., "Thermomechanical Analysis of Porous Solid Oxide Fuel Cell by using Peridynamics," *AIMS Energy*, 5(4), pp.585-600 (2017).
9. S. Plimpton, "Fast Parallel Algorithms for Short-Range Molecular Dynamics," *Journal of Computational Physics*, 117, pp.1-19 (1995).
10. Parks, M. L., Lehoucq, R. B., Plimpton, S. J. and Silling, S. A., "Implementing Peridynamics within a Molecular Dynamics Code," *Computer Physics Communications*, 179(11), pp.777-783 (2008).
11. Kirsch, C., „Die Theorie der Elastizität und die Bedürfnisse der Festigkeitslehre," *Zeitschrift des Vereines Deutscher Ingenieure*, 42, pp.797-807 (1898).
12. Tada, H., Paris, P. C. and Irwin, G. R., *"The Stress Analysis of Cracks"*. Handbook, Del Research Corporation (1973).
13. Bolot, R., Qiao, J-H., Bertrand, G., Bertrand, P. and Coddet, C., "Effect of Thermal Treatment on the Effective Thermal Conductivity of YPSZ Coatings," *Surface and Coatings Technology*, pp.1034-1038 (2010).
14. Du-Ming Tsai, "A Fast Thresholding Selection Procedure for Multimodal and Unimodal Histograms," *Pattern Recognition Letters*, pp.653-666 (1995).
15. Wang, Z., Kulkarni, A., Deshpande, S., Nakamura, T. and Herman H., "Effects of Pores and Interfaces on Effective Properties of Plasma Sprayed Zirconia Coatings," *Acta Materialia*, 51, pp.5319-5334 (2003).
16. McPherson, R., "A Review of Microstructure and Properties of Plasma Sprayed Ceramic Coatings," *Surface and Coatings Technology*, 39/40, pp.173-181 (1989).
17. Malzbender, J., Wakui, T., Wessel, E. and Steinbrech, R. W., "Fracture Behaviour of Plasma Sprayed Thermal Barrier Coatings," In *Fracture Mechanics of Ceramics*, Springer, Boston, MA, pp.421-435 (2005).
18. Zivelonghi, A., Cernuschi, F., Peyrega, C., Jeulin, D., Lindig, S. and You, J. H., "Influence of the Dual-Scale Random Morphology on the Heat Conduction of Plasma-Sprayed Tungsten via Image-Based FEM," *Computational Materials Science*, 68, pp.5-17 (2013).
19. Thurn, G., Schneider, G. A., Bahr, H. A. and Aldinger, F., "Toughness Anisotropy and Damage Behavior of Plasma Sprayed ZrO_2 Thermal Barrier Coatings," *Surface and Coatings Technology*, 123(2-3), pp.147-158 (2000).

(Manuscript received March 4, 2019,
accepted for publication Sepyember 14, 2019.)